POLITECNICO DI TORINO
Repository ISTITUZIONALE

Investigation of Cu-doped ceria through a combined spectroscopic approach: Involvement of different catalytic sites in CO oxidation

(Article begins on next page)

27 April 2024

Investigation of Cu-doped ceria through a combined spectroscopic approach: involvement of different catalytic sites in CO oxidation

Enrico Sartoretti[a]*, Chiara Novara[a], Maria Cristina Paganini[b], Mario Chiesa[b], Micaela Castellino[a], Fabrizio Giorgis[a], Marco Piumetti[a], Samir Bensaid[a], Debora Fino[a], Nunzio Russo[a]

[a] Department of Applied Science and Technology, Politecnico di Torino, Corso Duca degli Abruzzi, 24, 10129 Turin, Italy.

[b] Department of Chemistry and NIS, University of Turin, Via Pietro Giuria, 7, 10125 Turin, Italy.

* Corresponding author:

   E-mail address: enrico.sartoretti@polito.it (Enrico Sartoretti)

ABSTRACT

Copper-ceria mixed oxides are widely considered promising catalysts for oxidation reactions, especially when the participation of lattice oxygen is required. However, the mechanistic understanding of these catalytic systems is still incomplete, due to their considerable complexity. In fact, copper doping of ceria results in the formation of a significant number of different interacting sites in continuous evolution during the catalytic processes. In the present study, pure and Cu-doped ceria samples were deeply investigated through combined spectroscopic techniques, i.e. XPS, EPR, and in situ FTIR and Raman spectroscopy. Through this systematic approach, the copper sites and lattice defects responsible for the enhanced CO oxidation activity of doped ceria were elucidated. Superficial Cu^+ species and small Cu^0 clusters promote the adsorption of CO at low temperature, while isolated Cu^{2+} monomers and dimers well-dispersed in the ceria matrix foster lattice oxygen mobility, involving the sub-surface in the redox phenomena. Consequently, the structure of Cu-doped ceria undergoes substantial modifications throughout CO oxidation in the absence of O_2, with the formation of oxygen vacancy clusters. Anyway, these changes are reversible, and structural reorganization in the presence of O_2 can occur even at room temperature. The excellent performance of Cu-doped ceria eventually stems from the effective cooperation among the different catalytic sites in the mixed oxide.

1. Introduction

Cerium oxide is a well-known heterogeneous catalyst fruitfully employed in various applications. Thanks to its peculiar redox properties, this material is able to effectively promote different reactions, such as the abatement of gaseous pollutants or particulate matter, the preferential oxidation of CO, the water gas shift reaction, methane dry reforming, as well as several photocatalytic or electrocatalytic processes [1–10]. The properties of ceria-based catalysts can be finely tuned not only by optimizing the synthesis procedure but also by selecting proper dopants, in order to maximize the final performances [11]. Indeed, the incorporation of foreign elements in ceria fluorite structure can foster the formation of different kinds of lattice defects and promote the overall redox properties of the catalytic system [12–15].

In particular, ceria-copper catalysts have exhibited great potential as effective alternatives to the widely used supported noble metals, concurrently being much less expensive and more easily available [15–21]. However, despite the great interest aroused by Cu-Ce mixed oxides, their full mechanistic understanding has not been achieved yet, because of the considerable complexity of these systems. The strong interactions between ceria and copper leads to the formation of a highly variable structure, in which a considerable number of different interacting sites is in continuous transformation during the catalysis [5,22–24]. For instance, the simultaneous presence of Cu^0, Cu^+ and Cu^{2+} species in a CuO/CeO_2

catalyst during CO preferential oxidation was reported by Davó-Quiñonero et al. [20]. Both copper sites and lattice defects are directly involved in the redox phenomena and strongly promote oxygen mobility across ceria framework [13,25]. This is extremely beneficial for those reactions occurring through a Mars-van Krevelen (MvK) type mechanism, in which lattice O^{2-} ions act as the primary oxygen source, creating oxygen vacancies which are subsequently refilled by gaseous O_2 [15,20,22]. Such a behavior enables the use of doped ceria for catalyzing oxidation reactions in O_2 deficiency, e.g. in the three way catalysts for gasoline-fueled vehicles; in the latter case, an improved lattice mobility allows to draw more oxygen from the sub-surface and bulk of the catalyst when it is not available in the gas phase [26]. The structural flexibility of ceria-copper mixed oxides is also coupled to an almost full reversibility, resulting in long-term stability under reaction conditions [23,25,27,28].

Promising performances have been recently exhibited by well-defined Cu-doped ceria nanostructures prepared through hydrothermal synthesis [12,15,26,29,30]: indeed, the surface planes exposed by catalyst particles strongly affect phenomena such as the adsorption and activation of reactants, directly influencing the reaction efficiency [31]. In previous studies, the basic physico-chemical properties and the catalytic activity of such Cu-doped ceria-based materials have been investigated, and their defect chemistry has been thoroughly explored via in situ Raman spectroscopy, following the structural evolution during CO and soot oxidation [14,23]. Tests performed in different conditions allowed to unveil some unexpected mechanisms, such as the dissociative adsorption of CO in the presence of O_2, the formation of clusters of oxygen vacancies in reducing conditions, or the deactivation of reactive oxygen species at the catalyst surface by excessively concentrated oxygen vacancies during soot oxidation. However, little information was obtained about the role of copper sites during the catalysis. Hence, in the present work, novel in situ Raman analyses were combined with other spectroscopic techniques, such as high-resolution XPS, EPR, and in situ FTIR, with the aim of finally finding out which kinds of copper sites allow to boost ceria oxidizing activity. Thanks to this comprehensive approach, four different Cu species were detected in 5 at.% Cu-doped ceria nanoparticles, and the effects of these sites on the catalyst activity and defectiveness were discussed.

2. Materials and Methods

Pure (Ce100) and Cu-doped (Ce95Cu5) ceria was prepared through a hydrothermal synthesis procedure [14,29]. The 5 at.% Cu loading was chosen with the aim of creating a Ce-Cu solid solution and to avoid the segregation of big CuO particles. $Ce(NO_3)_3 \cdot 6H_2O$ and $Cu(NO_3)_2 \cdot 3H_2O$ (both provided by Sigma-Aldrich) were employed as metal precursors. In detail, a total of 20 mmol of nitrates (of which 19 mmol of cerium nitrate and 1 mmol of copper nitrate for the Ce95Cu5 sample) were dissolved in 10 mL of deionized water. This solution was then added dropwise to a second solution prepared by dissolving 48 g of NaOH (Sigma-Aldrich) in 70 mL of deionized water. After stirring at room temperature (RT) for 1 h, the thus obtained mixture was heated at 180 °C for 24 h in an autoclave. Subsequently, the sludgy precipitate was rinsed several times with ethanol and deionized water, in order to remove Na traces, and then it was dried at 70 °C overnight. Finally, the solid powder was gently crushed in a mortar and calcined in air at 550 °C for 4 h.

The actual copper content in the Ce95Cu5 sample was determined through inductively coupled plasma-mass spectrometry (ICP-MS) using a Thermo Scientific iCAP RQ ICP-MS apparatus. The catalyst powder was dissolved in a 1 M sulfuric acid + 0.5 M ascorbic acid aqueous solution, stirring at RT overnight.

X-ray diffraction (XRD) was carried out in a Philips X'Pert PW3040 diffractometer, using Cu Kα radiation ($\lambda = 1.5418 \times 10^{-10}$ m). The average crystallite size was estimated through the Scherrer's equation, using a LaB_6 calibration standard to correct the instrumental peak broadening.

The average properties of pores and the specific surface area (SSA) were studied via nitrogen physisorption, carried out in a Micromeritics Tristar II 3020, using the Barrett-Joyner-Halenda (BJH) and the Brunauer–Emmett–Teller (BET) methods. The catalyst powder was pretreated at 200 °C for 2 h in N_2 flow prior to the analysis.

The morphology of the two samples was investigated through field emission scanning electron microscopy (FESEM), using a Zeiss Merlin equipped with a Gemini-II column. For better images, the solid powder was previously coated with a 5-nm-thick Pt layer via sputter deposition. In addition, high resolution transmission electron microscopy (HRTEM) images were collected using a Thermo Scientific Talos F200X microscope operated at 200 kV, equipped with a detector

for energy dispersive X-ray spectroscopy (EDX). The sample powder was suspended in high-purity 2-propanol and subsequently drop-casted on the lacey carbon film of a gold support grid. The elemental distribution was investigated by acquiring EDX maps in scanning-transmission electron microscopy (STEM) mode.

X-ray photoelectron spectroscopy (XPS) analysis, of the catalyst powder, was carried out by using a PHI 5000 Versa Probe instrument, equipped with a monochromatic Al k-alpha X-ray source (1486.6 eV), while the obtained data were elaborated with Casa XPS Version 2.3.18 software. Longer acquisition times were used to detect the high resolution (HR) Cu 2p core-level spectrum, due to the low abundance of this element in the catalyst. The binding energy of the high resolution spectra was referred to the C 1s peak at 284.8 eV to compensate the surface charging effect.

EPR spectra have been recorded with a Continuous Wave (CW) Bruker EMX spectrometer operating at X-band (9.5 GHz), equipped with a cylindrical cavity at 100 kHz field modulation. The spectra have been recorded both at RT and in a bath of liquid nitrogen (-196 °C).

Temperature programmed reduction with hydrogen (H_2-TPR) was carried out in an Altamira Ami-300Lite instrument equipped with a thermal conductivity detector (TCD). The sample powder (50 mg) was pretreated in He at 550 °C for 30 min, than it was heated from 50 to 900 °C under a flow of 5% H_2 in Ar using a 10 °C min^{-1} ramp.

A Renishaw InVia Raman microscope was employed to collect Raman spectra of the samples in backscattering configuration, using a 514.5 nm excitation wavelength and a 5x objective. The RT Raman spectra were obtained averaging several spectra acquired in different regions of each sample, each one collected with a total exposure time of 225 s. After spectral deconvolution (with a procedure reported in [14]), the defect abundance of the catalysts was compared by calculating the ratio between the areas of the defect-induced bands (D1, D2 and D3 bands, located between 500 and 650 cm^{-1}) and the main F_{2g} peak of ceria (located around 465 cm^{-1}). The behavior of defects in the presence of CO was investigated through in situ Raman measurements, performed using a Linkam TS1500 cell. A small catalyst tablet, obtained by pressing the powder at 4 ton, was placed in the Linkam cell and kept in the desired atmosphere by flowing 45 mL min^{-1} of gas.

Fourier transform infrared (FTIR) spectra were collected in transmission mode in a Bruker Invenio S spectrometer equipped with a mercury-cadmium-telluride detector. Catalyst powder was pressed into a self-supporting wafer (with a $10 - 20$ mg cm^{-2} density) and then inserted in a suitable quartz cell with KBr optical windows. Before each analysis, the sample was outgassed in high vacuum ($5x10^{-4}$ mbar) at 400 °C for 30 min; in some cases, this pretreatment was followed by the exposure of the sample to CO (20 mbar) at 400 °C for 60 min. FTIR spectra were then acquired at RT with a resolution of 2 cm^{-1}. In situ measurements were carried out to investigate the interaction between the catalyst surface and CO or methanol molecules, by admitting increasing quantities of these species in the IR cell, up to a pressure of 10 mbar, acquiring a spectrum for each step of pressure.

CO oxidation was chosen as probe reaction to evaluate the catalyst activity, performing tests in isothermal mode. In brief, a fixed bed containing 100 mg of catalyst was inserted in a U-shaped quartz reactor placed in a furnace. During the test, the catalyst was kept under a 50 mL min^{-1} flow of a mixture of 1000 ppm of CO and 10% of O_2 in N_2.and the reactor outlet concentration of CO and CO_2 was measured employing an ABB Uras 14 continuous gas analyzer. Starting from 50 °C, the temperature was increased by 25 or 50 °C step by step, each time waiting for the establishment of a steady state (i.e. constant gas composition at the reactor outlet) before raising the temperature. Prior to the test, the catalytic bed was pre-treated at 100 °C for 30 min flowing a 50 mL min^{-1} flow of air.

3. Results and Discussion

3.1. Structural and textural properties of the catalysts

The structural properties of pure and Cu-doped ceria were investigated via XRD. The diffractograms of both samples were characterized by the typical reflections of CeO_2 fluorite structure (Fig. S1), while peaks related to copper-based segregated phases were not detected [16,17]. The latter observation suggests that most Cu ions are well-dispersed and directly incorporated in ceria lattice. As visible in Table 1, this is reflected on a lower average crystallite size for the doped sample.

The lower dimension of crystals and particles in the Ce95Cu5 sample is also responsible for its quite higher specific surface area and pore volume (Table 1), and it was confirmed via electron microscopy. Furthermore, Cu addition caused a remarkable change of the catalyst morphology. As clearly displayed by the FESEM and TEM micrographs in Fig.1, pure ceria mainly consists of well-defined nanocubes, with variable dimensions ranging from 20 to 400 nm; instead, the Ce95Cu5 sample is made of faceted nano-polyhedra, exhibiting a more rounded shape and a lower dimension between 5 and 30 nm. The analysis of the fringes in HRTEM images revealed that the nanoparticles of both the samples are single crystals, independently on their particular morphology; furthermore, they are all characterized by the typical ceria fluorite structure, in agreement with XRD and with previous studies [23]. No particles exhibiting a different crystal structure were found while analyzing the Ce95Cu5 sample, suggesting that segregated copper domains (such as CuO nanoparticles) are absent. This indication was confirmed by collecting STEM-EDX maps on the mixed oxide (one of them is reported in Fig. 1): the elemental microanalysis indeed evidenced that Cu is homogenously distributed across the Ce95Cu5 sample, while no Cu aggregates were detected.

Table 1

Structural properties of the Ce100 and Ce95Cu5 catalysts (in line with those of analogous hydrothermally-synthesized samples reported in [29]).

Catalyst	D_C [a] (nm)	SSA [b] ($m^2 g^{-1}$)	V_p [b] ($cm^3 g^{-1}$)	D_p [b] (nm)
Ce100	144	7	0.05	30
Ce95Cu5	20	39	0.14	11

[a] The average crystallite size (D_C) was estimated using XRD data
[b] The specific surface area (SSA), the total pore volume (V_p) and the average pore diameter (D_p) were measured through N_2-physisorption
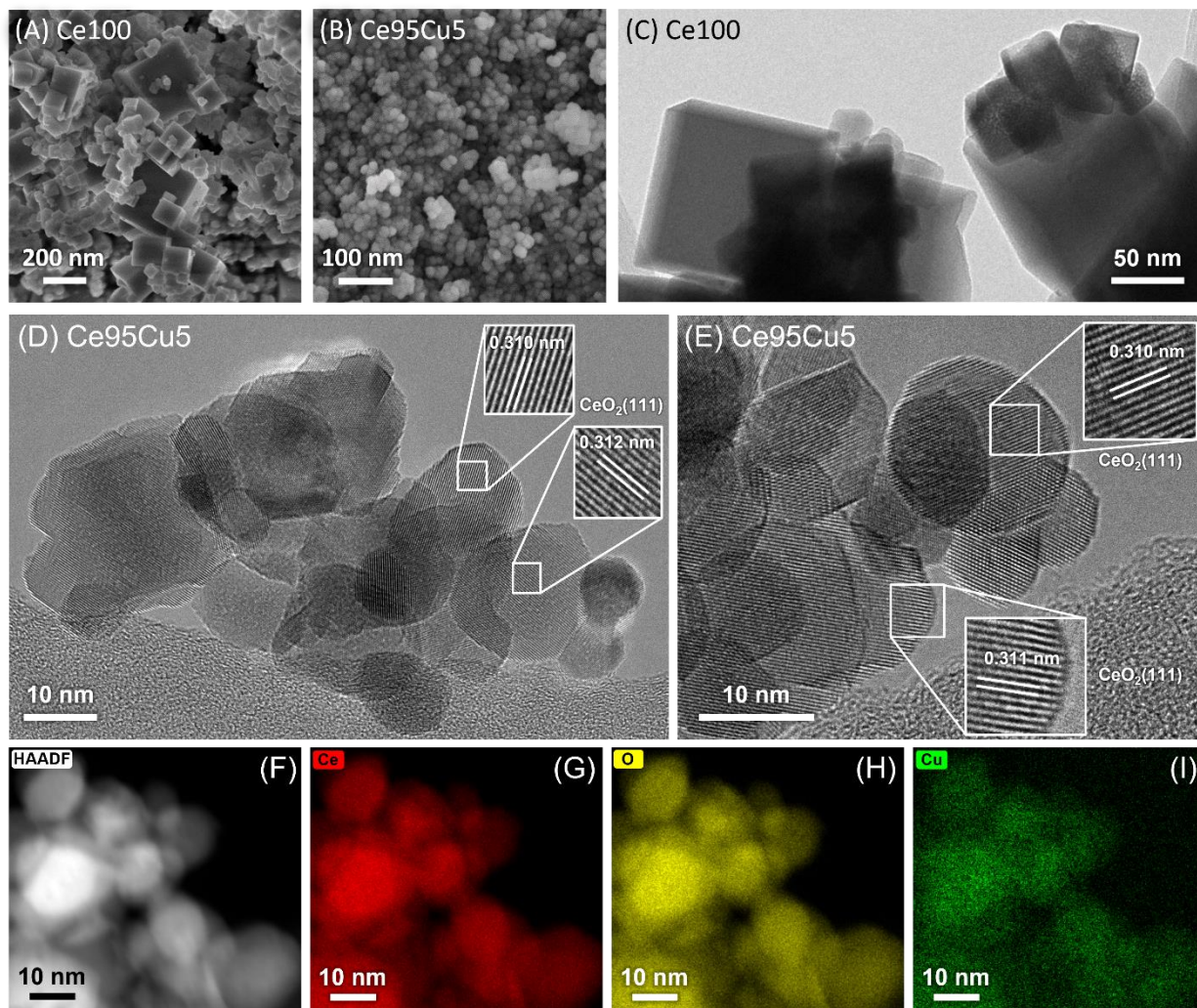
Fig. 1. FESEM images of the Ce100 (A) and Ce95Cu5 (B) catalysts. Bright field image of Ce100 (C) and HRTEM images of Ce95Cu5 (D, E). EDX map collected in STEM mode on the Ce95Cu5 sample: high-angle annular dark-field image of the investigated area (F) and distribution of Ce (G), O (H) and Cu (I).

3.2. Chemical properties of the catalysts

The composition and oxidation state of the catalyst surface was examined through XPS, whose main results are reported in Table 2. In the O 1s XPS spectra (Fig. S2 A), two distinct peaks were identified. The main peak around 528.8 eV can be ascribed to lattice oxygen (O_β), while the less intense peak at 531.0 eV is related to the presence of various capping oxygen species (O_α) [32,33]. The two samples exhibit a very similar relative abundance of O_α and O_β.

The deconvolution of Ce 3d XPS spectra (Fig. S2 B), performed with a procedure adapted from [34], allowed to quantify the amount of reduced cerium. In detail, two sets of signals can be identified concerning the Ce 3d core level: five "v" peaks are related to Ce $3d_{5/2}$ level, while five "u" peaks correspond to the Ce $3d_{3/2}$ state. Among them, four features (v°, v', u° and u') can be ascribed to Ce^{3+} ions, while the other six components can be referred to the 4+ oxidation state [35]. As can be seen in Table 2, the Ce95Cu5 catalyst exhibits a slightly higher quantity of Ce^{3+} ions at its surface with respect to pure ceria. The higher degree of reduction of the material is due to the charge transfer between Cu and neighboring Ce^{4+} ions occurring upon Cu incorporation in ceria lattice [13,36].

Furthermore, XPS detected the presence of 5.6 at.% of copper in the Ce95Cu5 catalyst (with respect to the total amount of Ce + Cu ions), which is rather similar to the nominal copper loading (5 at.%) and to the actual copper loading measured via ICP-MS (4.5 at.%). This suggests that Cu ions are well distributed in the ceria matrix, whereas the

preferential massive segregation of copper on the ceria surface can be ruled out. The high resolution XPS spectrum of Cu 2p doublet (Fig. S3 A) was characterized by a main peak at 932.4 eV and by a much weaker feature around 952.0 eV, which corresponds to Cu $2p_{1/2}$ component; at the same time, satellite peaks, which would mark the presence of Cu^{2+} species, were absent in the spectrum [37]. Moreover, a Cu LMM Auger peak located at 916.6 eV in the kinetic energy scale was detected (Fig. S3 B), and this feature can be attributed to Cu^+ species [38]. The combination of these two results reveals that surface copper is mainly in the Cu^+ state [39], while eventual Cu^{2+} or Cu^0 sites are too few to be effectively detected by XPS. Cu^+ species at ceria surface are believed to be good active sites for CO adsorption and oxidation [15,40,41].

Table 2

Relative abundance of the surface species in the two catalysts obtained via XPS (in line with those of analogous hydrothermally-synthesized samples reported in [29]).

Catalyst	Oxygen species (%)		Cerium species (%)	
	O_α	O_β	Ce^{3+}	Ce^{4+}
Ce100	33.2	66.8	22.5	77.5
Ce95Cu5	33.5	66.5	24.3	75.7

The chemical properties of the two catalysts were further investigated via EPR. The EPR spectrum of pure ceria (Fig. S4) is characterized by a single low-intensity signal at around 345 mT, which could be due to the presence of some impurities or to electrons trapped near the surface of Ce^{3+}/Ce^{4+} redox pairs [42]. Ce^{3+} is a paramagnetic ion with one unpaired electron in the 4f orbital, however due to unfavorable relaxation times, it is usually EPR silent at T > 4 K. On the contrary, a distinct EPR signal due to the presence of Cu^{2+} species is observed in the Ce95Cu5 sample (Fig. 2 A). The spectrum can be interpreted as the superposition of monomeric Cu^{2+} centers (S=1/2) and ferromagnetically coupled Cu^{2+} dimers (S=1) [13,43–45]. The dimer spectrum is characterized by a complex powder pattern featuring, for each fine transition, seven hyperfine lines with relative intensities 1:2:3:4:3:2:1, resulting from the coupling of the total electron spin to the Cu magnetically active nuclei (natural abundance ^{63}Cu 69.15%, ^{65}Cu 30.85%, both $I = 3/2$). The half-field peaks, observed at approximately 160 mT, can be attributed to a double quantum transition ($\Delta_{ms} = \pm2$) of the coupled-spin system (see the inset in Fig.2 A) [46,47].The spectrum assigned to the isolated ionic Cu^{2+} species (i.e. isolated monomers) is characterized by four narrow and structured lines around 330 mT ($g_\perp = 2.045$) while the corresponding $g_{//}$ region ($g_{//} = 2.221$) is less defined and structured. The presence of these isolated Cu species is indicative of the formation of a solid solution between ceria and copper [43].

Being oxygen a paramagnetic molecule, in the presence of other paramagnetic species we can observe an interaction among the paramagnetic surface species and molecular oxygen, resulting in the quenching of the EPR signal. If the EPR active species are in the bulk of the sample, no interaction with oxygen is observed and the EPR signal is not affected by the presence of molecular oxygen. In this case, experiments carried out on the Ce95Cu5 catalyst in the presence of molecular oxygen (S=1) showed no change in the spectral linewidth of both isolated monomers and ferromagnetically coupled dimers, indicating that these species are located in the bulk of the sample and are not affected by spin-spin interactions. This observation confirms the good dispersion of copper inside the ceria framework, and is consistent with the failure to detect Cu^{2+} in the surface of the Ce95Cu5 catalyst. In fact, the absence of the typical Cu^{2+} satellite in the Cu 2p XPS spectrum of this sample (Fig. S3 A) is probably due to the too low abundance (below XPS sensitivity) of this oxidation state in the most superficial layers of the catalyst particles.

EPR spectra were also collected after treating the Ce95Cu5 catalyst with different gases at high temperature. In Fig. 2B the spectra obtained after a thermal treatment in presence of N_2 (Fig 2B_b) and O_2 (Fig 2B_c), performed at 400 °C for 30 min, are shown. The thermal treatment in the presence of molecular nitrogen leads to a reduced intensity of the Cu^{2+} signals, indicating a partial reduction of the Cu^{2+} species in line with other characterization techniques (XPS and FTIR). On the contrary, in the presence of molecular oxygen, the intensity of Cu^{2+} EPR signal increases, indicating the oxidation of EPR silent Cu^+ species at the surface.
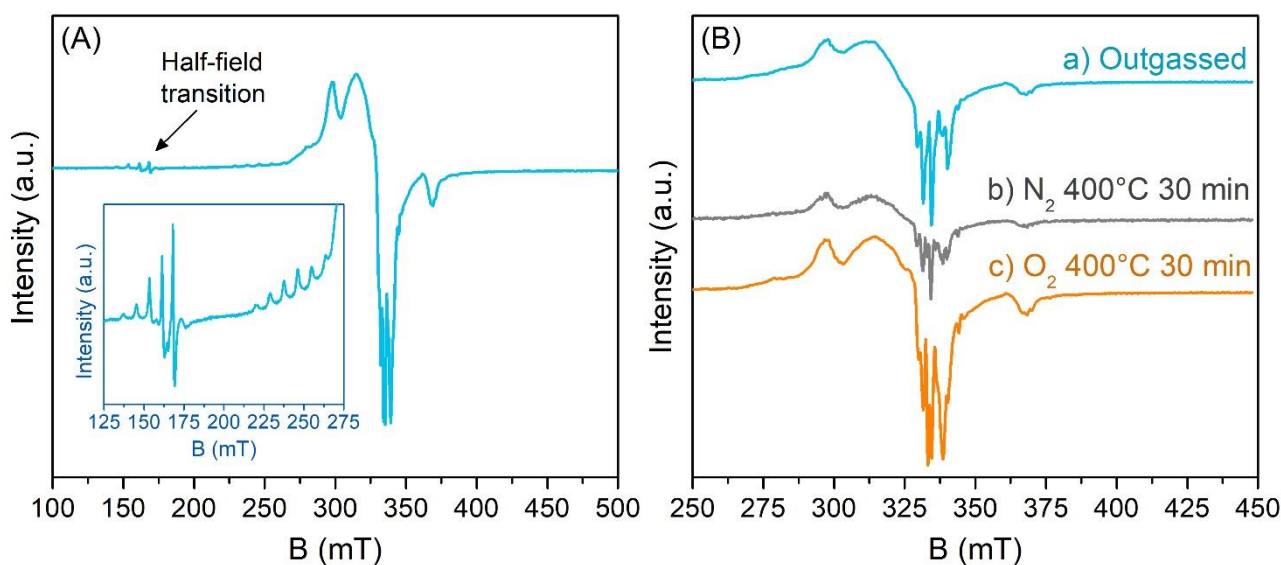
Fig. 2. Complete EPR spectrum of the Ce95Cu5 sample acquired at 77 K after outgassing the powder (A); in the inset, the half-field transition region is magnified. EPR spectra collected at 77 K after treating the Ce95Cu5 catalyst in different ways (B): after outgassing the sample (a), after thermal treatment in N_2 at 400 °C for 30 min (b), and after thermal treatment in O_2 at 400 °C for 30 min (c).

The material reducibility, which is a key aspect in the case of oxidation catalysts [48], was further evaluated through H_2-TPR, whose profiles are reported in Fig. 3. The reduction of pure ceria occurs in two steps, corresponding to the two peaks in the TPR curve: the surface is reduced around 550 – 600 °C, while the oxide bulk is reduced at higher temperatures, above 700 °C [12,49]. Two analogous peaks can be observed for Ce95Cu5 as well, albeit at lower temperatures (i.e. around 440 °C and 850 °C); this means that both the surface and the bulk of the mixed oxide can reduce more easily with respect to pristine ceria. Moreover, an additional low temperature peak at about 250 °C is linked to the reduction of copper species, which also involves the simultaneous reduction of Ce^{4+} ions strongly interacting with Cu sites. As a whole, Cu doping does not only promote ceria reducibility in terms of lower temperature required, but it also increases the quantity of Ce ions participating in the redox cycle. In fact, the specific hydrogen consumption during TPR (reported in Table S1) is significantly higher for the doped sample (+23% compared to pure ceria), especially when the surface reduction is considered. This enhanced redox behavior can be expected to boost the MvK mechanism, thereby improving the oxidizing activity of the catalyst.
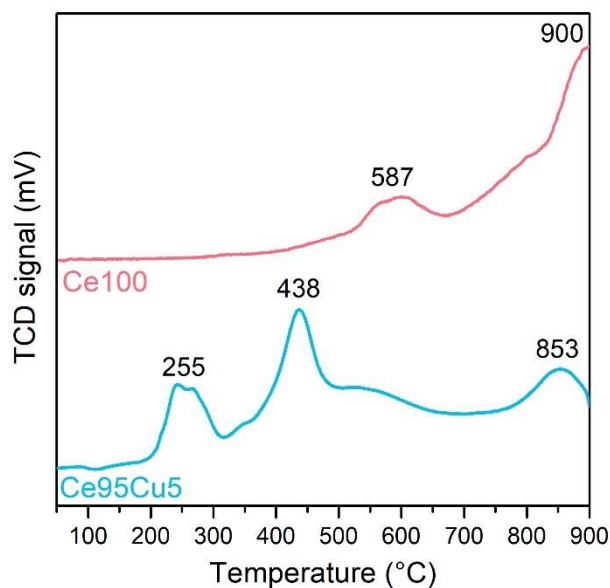
Fig. 3. H$_2$-TPR profiles of the two catalysts.

3.3 Investigation of defect sites

Raman spectroscopy is a widely employed technique to study the defect sites in ceria-based materials, thanks to its high sensitivity to lattice distortion [50]. The Raman spectra collected at RT on the Ce100 and Ce95Cu5 catalysts are displayed in Fig. 4. The spectrum of Ce100 is dominated by a prominent sharp F$_{2g}$ peak at about 465 cm^{-1}, which arises from the symmetric stretching of Ce – O bonds in ceria fluorite structure [23,50]. A further Raman component (D1) can be found at 598 cm^{-1}, and it can be ascribed to the presence of intrinsic anionic Frenkel sites, involving the displacement of O^{2-} ions in interstitial position [14,51].

Upon Cu addition, no features directly related to the presence of copper oxide appear in the Raman spectrum [17,52], confirming the absence of significant copper segregation. Nevertheless, both the ceria F$_{2g}$ peak and the defect-related band are subjected to significant changes. The main peak of the Ce95Cu5 sample is broader and red-shifted to 459 cm^{-1}, as a result of structural distortion due to Cu insertion in ceria lattice. At the same time, the defect band (D band) gains intensity and two new components appear beside the D1 peak linked to Frenkel pairs (595 cm^{-1}), as depicted in the inset of Fig. 4. A D2 signal at 625 cm^{-1} has been previously assigned to oxidized substitutional sites not containing oxygen vacancies [23,53]. Moreover, a less intense D3 component located at 552 cm^{-1} is usually attributed to oxygen vacancies (O$_V$), such as those accompanying Ce^{3+} ions or other aliovalent cations inserted in ceria lattice [54]. The presence of this feature in Cu-doped ceria may result from Cu incorporation and from the conspicuous quantity of reduced cerium pointed out by XPS. However, a previous study carried out on analogous materials revealed that the D3 component is only visible in certain conditions, suggesting its assignment to clusters of oxygen vacancies [23]. In detail, in situ Raman measurements detected an intense and broad D3 band at high temperature in reducing conditions (400 °C, 1000 ppm CO/N$_2$); unexpectedly, the latter component promptly disappeared when the sample was cooled down or when CO was removed from the atmosphere, despite the absence of gaseous O$_2$ able to refill the vacancies. Nevertheless, a structural reorganization from O$_V$ clusters to isolated O$_V$ can account for this behavior, supporting the attribution of the D3 defect band to clustered vacancies. In the Ce95Cu5 sample, the formation of oxygen vacancy clusters may be associated with the presence of the Cu^{2+} dimers detected via EPR.

Defect abundance can be evaluated by considering the ratios between the areas of the defect peaks and the one of the F$_{2g}$ component [55,56], which are reported in Table 3. The total amount of defects in the ceria lattice (proportional to the D/F$_{2g}$) remarkably increases upon Cu doping, due to both the rise of the intrinsic Frenkel sites and the generation of new extrinsic sites (i.e. substitutional sites and oxygen vacancies). The higher defectiveness of the Ce95Cu5 sample, which is linked to the good Cu incorporation, contributes to the superior catalytic activity of this sample towards CO oxidation [23,30].

8
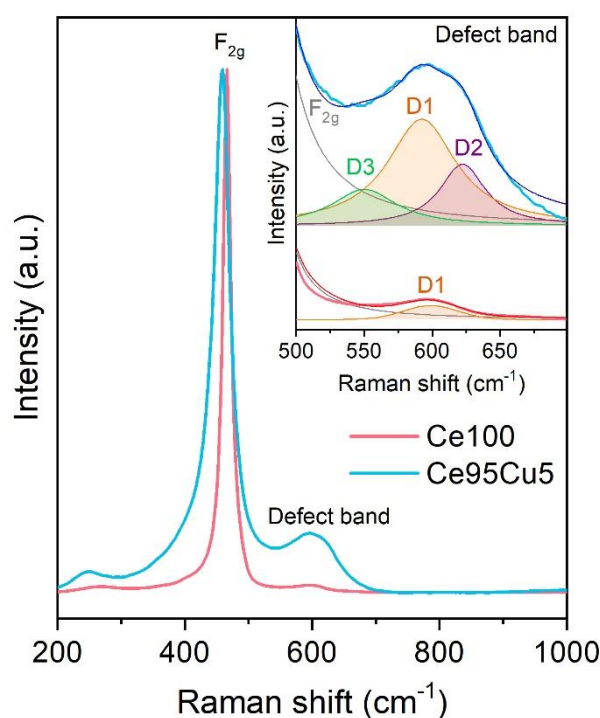
Fig. 4. Raman spectra of the two catalysts collected at RT, normalized to the F_{2g} peak intensity. In the inset, the defect band is magnified, highlighting the different deconvolved peaks (thin lines).

Table 3

Ratios between the area of different Raman peaks in the spectra collected at RT (in line with those of analogous samples reported in [14]).

Catalyst	D1/F_{2g}	D2/F_{2g}	D3/F_{2g}	D/F_{2g}
Ce100	0.021	-	-	0.021
Ce95Cu5	0.168	0.064	0.054	0.286

Further insights into the distribution of oxygen vacancies were provided by in situ FTIR measurements. Actually, the FTIR analysis of methanol adsorption has proved to be a valuable technique for the investigation of the outermost surface of ceria-based materials and of its active sites [57–61]. Hence, methanol was used as probe molecule during dedicated FTIR tests. After an outgassing pretreatment of the catalyst at high temperature, methanol vapor was gradually admitted to the FTIR cell; the spectra collected while increasing step by step the partial pressure are presented in Fig. 5 A and B (full spectra in Fig. S5). In general, a higher quantity of adsorption sites was found for Ce95Cu5, due to the higher surface area of this sample. For both the catalysts, three main ν(C–O) stretching modes progressively appeared in the FTIR spectra, signaling the formation of different methoxy species as a result of methanol dissociative adsorption over ceria surface. All these components exhibited a gradual blue-shift linked to the increasing coverage of the adsorption sites. In detail, the peak at 1106 cm^{-1} is ascribed to methoxy groups on-top of Ce^{4+} cations (type I) [58,59], while the two bands at around 1050 cm^{-1} and 1075 cm^{-1} are related to two types of bridging methoxy (type II and II') forming on different surface planes (i.e. (110) and (100) planes, respectively) [60]. A shoulder around 1015 cm^{-1}, attributed to triple-bridging methoxy (type III), was barely detected in the FTIR spectra of Ce95Cu5 acquired at low methanol dosing. A weak component at 1034 cm^{-1} (a sharp peak for Ce100, a shoulder for Ce95Cu5) also appeared at high pressure, deriving from methanol physisorbed on the surface [60]. Interestingly, in the intermediate-pressure spectra of both the samples no peaks are present in the 1030 – 1035 cm^{-1} region., which would have been assigned to bridge methoxy in proximity of an oxygen vacancy [59,60]. The absence of such a signal may therefore mean that

9

oxygen vacancies in these ceria-based catalysts are not easily accessible to methanol at RT, suggesting that most of them might be located in the oxide bulk or at least in a sub-surface layer.
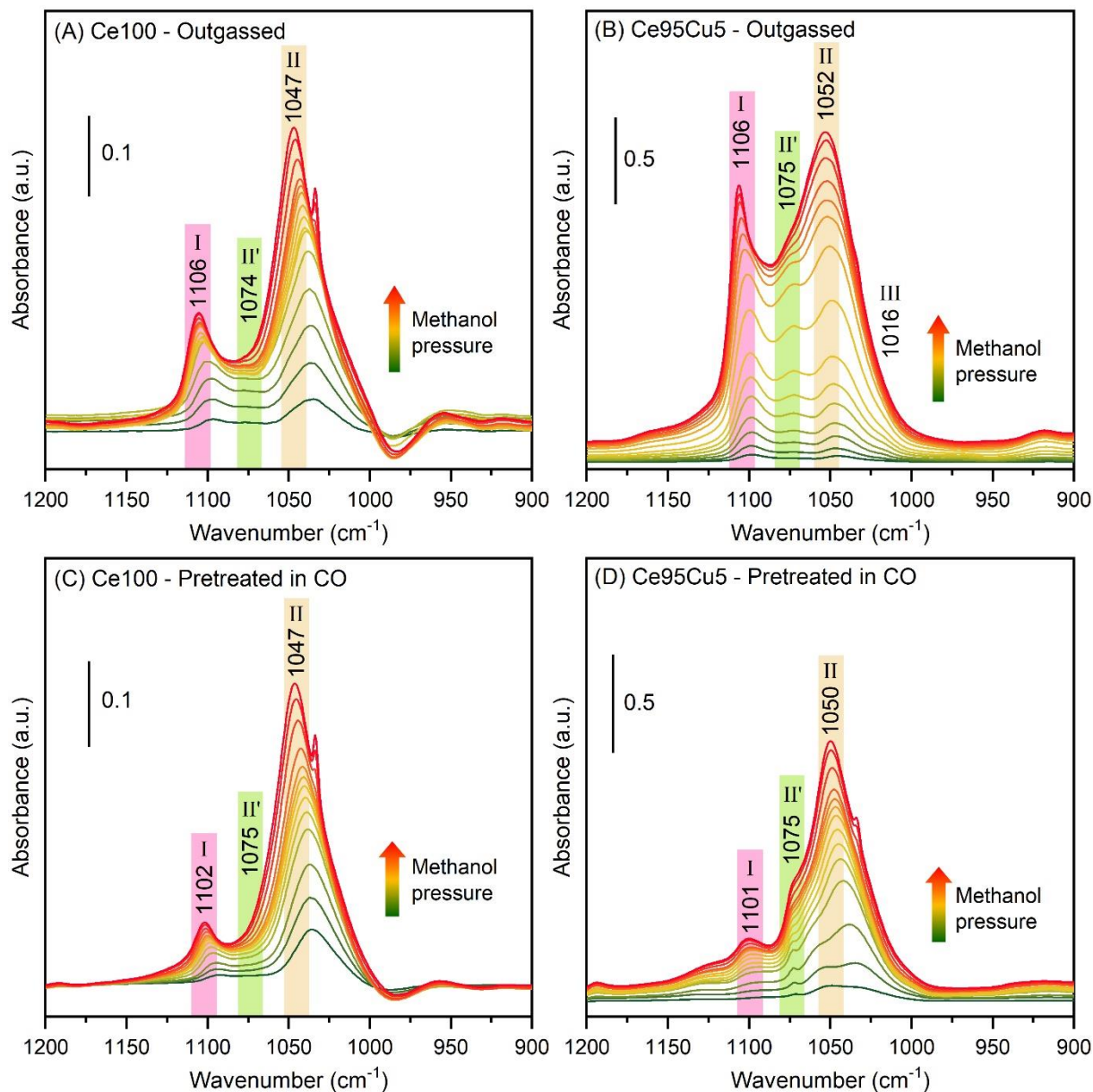
Fig. 5. In situ FTIR spectra collected at RT during methanol adsorption on the Ce100 (A, C) and Ce95Cu5 (B, D) catalysts. Prior to the analysis, the samples were outgassed at 400 °C for 30 min (A, B), or they were outgassed, reduced in CO at 400 °C for 1 h and then outgassed again (C, D). During the measurements, an increasing quantity of methanol was gradually admitted to the FTIR cell by raising its partial pressure from 0.01 mbar (green line) to 10 mbar (red line). The spectrum acquired on the clean sample before starting the analysis was subtracted from the other ones to better highlight the differences. The spectra were then normalized with respect to the thickness of each sample tablet.

The same analysis was repeated on samples subjected to a reducing pretreatment with CO at 400 °C (Fig. 5 C and D). Concerning pure ceria, the previous reduction does not affect the formation of bridge methoxy groups, but a slightly lower amount of type I methoxy species was detected. Instead, methanol adsorption on Ce95Cu5 is hindered by the surface reduction, and the abundance of on top methoxy drops as a consequence of the lack of Ce^{4+} capping ions. However, the feature of methoxy groups adsorbed in the vicinity of an oxygen vacancy was still not detected.

3.4. Catalytic activity for CO oxidation

CO oxidation was chosen as probe reaction to compare the oxidation activity of the two samples. Catalytic tests were performed in isothermal mode, i.e. sampling a sequence of steady states at increasing temperature (so that transient CO adsorption or desorption can be ignored). The CO conversion curves in Fig. 6 clearly point out the promoting effect of Cu as a dopant. Indeed, the Ce95Cu5 sample is able to reach the 50% of CO conversion ($T_{50\%}$) at about 150 °C, i.e. more than 200 °C before Ce100 ($T_{50\%}$ = 370 °C). Moreover, the mixed oxide achieves complete CO oxidation at 250 °C, while Ce100 requires more than 500 °C.

The huge difference between the performances of Ce100 and Ce95Cu5 is the result of the previously discussed effects of Cu addition on ceria physico-chemical properties. In particular, the abundance of defect sites in ceria-based materials has been directly correlated with the CO oxidation activity [15,23,29]. The insertion of copper sites in ceria lattice and the consequent weakening of the Ce – O bonds is also responsible for an increased lattice oxygen mobility, which allows a continuous supply of oxygen species to the surface, ensuring a fast reduction-oxidation mechanism. The latter reaction pathways is also promoted by the coupling of the Ce^{3+}/Ce^{4+} and Cu^{2+}/Cu^{+} redox cycles [62]. Finally, the presence of Cu^{+} cations at the catalyst surface promotes CO adsorption [15,40,41], as well as molecular oxygen activation [63].

The spent Ce95Cu5 catalyst obtained after performing CO oxidation at 250 °C was cooled down in inert atmosphere and characterized to find out eventual changes in its properties. Concerning the catalyst structure, no appreciable variations could be observed: the XRD pattern of the spent sample is unchanged (Fig. S6), as well as the average crystallite size (20 nm) and the specific surface area (40 m^2 g^{-1}). HRTEM investigations confirmed the presence of a solid solution, with Cu atoms homogeneously incorporated in the ceria lattice (Fig. S7), excluding the segregation of copper under operating conditions. Moreover, no evident change of the chemical state of superficial copper after the reaction was observed via XPS (again, only Cu^{+} could be detected, as shown in Fig. S8). This reversibility is in line with the excellent stability usually shown by hydrothermally-synthesized ceria-copper systems [15,26].
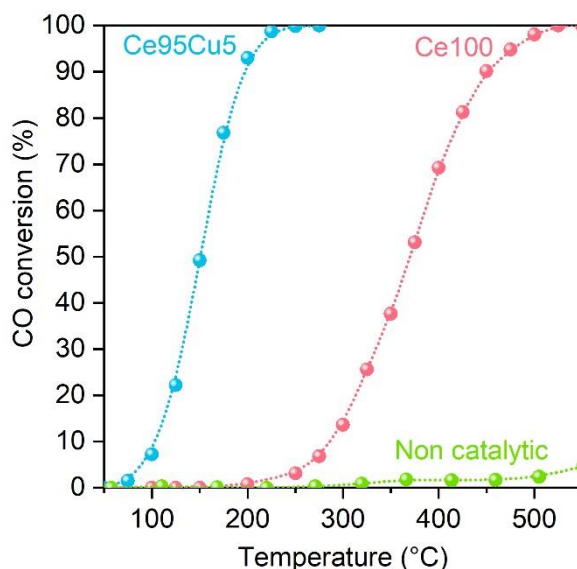

Fig. 6. Light-off curves reporting the percentage of CO converted as a function of the temperature during CO oxidation tests (feed gas mixture containing 1000 ppm of CO and 10% of O_2 in N_2, temperature increased step by step). Results are similar to those of analogous hydrothermally-synthesized samples described in [29].

The interactions between the two catalysts and CO were further investigated through in situ spectroscopy. In detail, CO adsorption phenomena were monitored by collecting FTIR spectra while the samples were exposed to increasing quantities of CO. No relevant changes were detected in the FTIR spectrum of Ce100 (see Fig. S9), indicating that CO does not significantly adsorb on pure ceria at RT. Instead, CO adsorption occurred at the surface of the Ce95Cu5

catalyst, as evidenced by the FTIR spectra in Fig. 7 A. Two main features appeared in the presence of CO, and their intensity rose while increasing CO partial pressure. The prominent peak at 2090 cm^{-1} results from adsorption of CO in linear configuration on superficial Cu$^+$ cations [40,62,64,65], which were also previously detected by XPS. The shoulder around 2073 cm^{-1} arises instead from the formation of Cu^0-carbonyl [62,65–67], signaling the presence of a few metallic Cu sites. Manzoli et al. ascribed an analogous band to CO adsorbed on very small Cu^0 clusters in close contact with a reduced cerium ion; these sites, which are stable and highly well-dispersed, are also suitable for oxygen activation at low temperature [66]. The spectral evolution in Fig. 7 A suggests that Cu^0 species at the surface of the Ce95Cu5 sample are quite scarce, since they are almost fully saturated by CO at low partial pressure; conversely, the continuously increasing intensity of the Cu$^+$-carbonyl feature points out the presence of a greater amount of superficial Cu$^+$ sites, which can be progressively occupied by CO molecules while the partial pressure of CO rises. Both Cu$^+$ and Cu^0 species were also detected in the unpretreated Ce95Cu5 sample (see Fig. S10), confirming that they do not simply form during the outgassing pretreatment at 400 °C.

In situ FTIR measurements of CO adsorption were repeated on Ce95Cu5 previously subjected to a reducing pretreatment in CO at 400 °C. As can be seen in Fig. 7 B, the peak at 2072 cm^{-1} gained relative intensity after this treatment, especially at low CO pressure, signaling an increase in the quantity of metallic Cu sites. However, a significant Cu$^+$ – CO feature was still present, even if less intense and slightly red-shifted (2087 cm^{-1}), indicating that only a partial reduction of Cu$^+$ occurred during the reducing pretreatment. The retention of copper in a partially oxidized state may be the result of the strong interactions between copper and ceria, which facilitate oxygen transfer. Interestingly, FTIR measurements performed on the spent Ce95Cu5 catalyst revealed that Cu$^+$ sites are still present after the reaction, while Cu^0 clusters were no more clearly detected (Fig. 7 C). This result suggests that the few Cu^0 sites at the catalyst surface are oxidized to Cu$^+$ under reaction conditions in abundance of O$_2$.
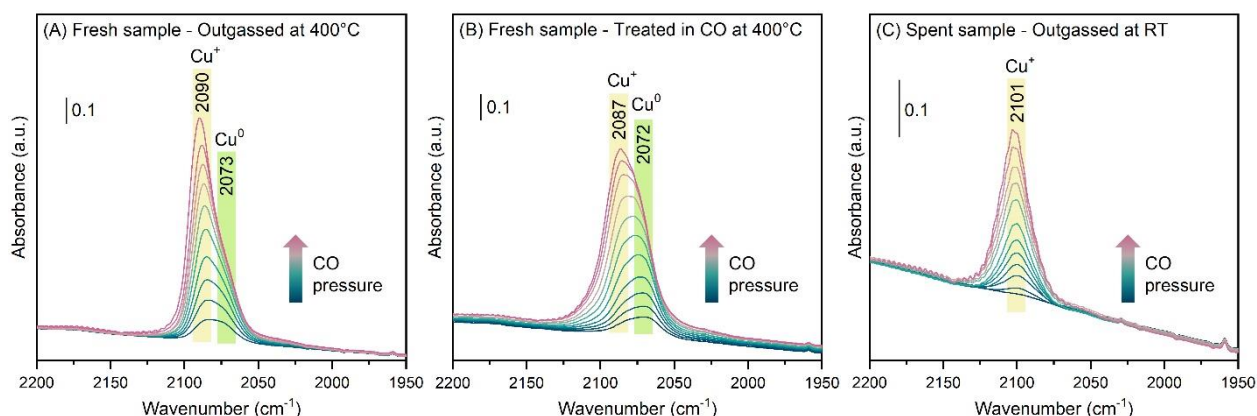
Fig. 7. In situ FTIR spectra collected at RT during CO adsorption on the Ce95Cu5 catalyst after different treatments: fresh catalyst outgassed at 400 °C for 30 min (A); fresh catalyst outgassed, reduced in CO at 400 °C for 1 h and then outgassed again (B); spent catalyst after CO oxidation, outgassed at RT for 30 min (C). During the measurements, an increasing quantity of CO was gradually admitted to the FTIR cell by raising its partial pressure from 0.01 mbar (blue line) to 10 mbar (pink line). The spectra were normalized with respect to the thickness of the sample tablet.

The behavior of oxygen vacancies and defects in the presence of CO was instead explored through a set of in situ Raman measurements. Briefly, the catalyst was heated at 400 °C in an inert flow and then exposed to 250 ppm of CO in N$_2$, waiting 60 min to detect the effects of the reduction over time. Afterwards, the cell was flushed with air and then with nitrogen, before sending a higher concentration of CO/N$_2$ for 60 min. This procedure was repeated multiple times, raising the CO concentration up to 1000 ppm, then the sample was cooled down to RT keeping the CO/N$_2$ atmosphere. Finally, air was admitted to the cell and its interaction with the catalyst was observed.

In line with previous experiments carried out on ceria nanocubes [23], the Ce100 sample did not exhibit any change in its Raman spectrum during exposure to increasing concentrations of CO (not even up to 1800 ppm, see Fig. S11 A). Additionally, no variations were observed in the spectra collected at RT before and after the test, which are completely overlapping (Fig. S11 B). Hence, ceria structure exhibits a remarkable stability, regardless of the presence of CO or O$_2$.

Conversely, substantial changes in the defect band characterize the Raman spectra of the Ce95Cu5 sample, as shown in Fig. 8. Actually, the exposure to a low CO concentration (250 ppm) does not cause appreciable alterations (Fig. 8 A). Anyway, CO oxidation over ceria in the absence of O_2 always entails the formation of O_V, which should directly reflect on a rise of the D band in the Raman spectrum. However, such a trend was not detected here: it can be therefore inferred that the presence of few O_V does not significantly contribute to the D3 band signal (i.e. the one around 550 cm^{-1} ascribed to O_V). This is in line with previous observations and with the assignment of the D3 band to O_V clusters [23]: in fact, when the superficial oxygen consumption is low, lattice oxygen can be transferred to the surface and then to CO without causing excessive structural distortion.

Instead, the situation changes at higher CO concentrations (Fig. 8 B, C and D): in these conditions, the defect band starts to vary as soon as CO is sent on the sample, acquiring a flatter shape as a result of an increase of the D3 component. The rise of the D3 intensity over time during exposition to CO is gradual and proceeds until a plateau is reached. Interestingly, by raising the CO concentration, the defect band growth becomes faster and, at the same time, a higher final intensity is achieved after 60 min (a direct comparison is displayed in Fig. 8 E). This suggests that different steady states are established depending on the quantity of CO in the gas. A higher CO concentration entails a higher oxygen demand at the catalyst surface: hence, the formation of O_V is accelerated, with creation of clusters, until a maximum is reached.
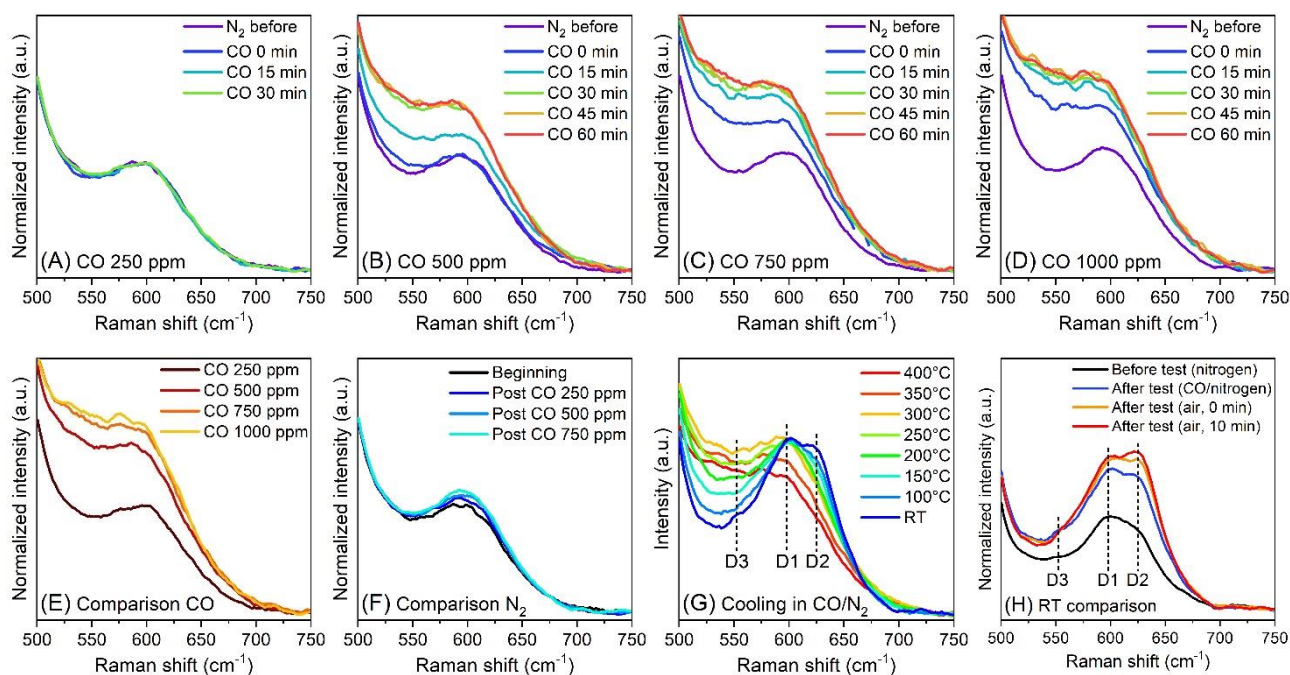
Fig. 8. Magnification of the defect band of in situ Raman spectra collected on the Ce95Cu5 sample in different conditions. Spectra acquired at 400 °C over time while flowing a mixture containing 250 ppm (A), 500 ppm (B), 750 ppm (C), or 1000 ppm (D) of CO in N_2. Comparison of the spectra recorded at 400 °C after 60 min of exposure to different concentrations of CO (E). Comparison of the spectra collected at 400 °C while flushing the cell with pure N_2 before and after exposure to different concentrations of CO (F). Spectra acquired at different temperatures while cooling down the sample after the test, under an atmosphere of 1000 ppm of CO in N_2 (G). Comparison of the spectra collected at RT in different atmospheres before and after the test (H).

Upon flushing the sample with air and nitrogen, the spectrum reacquires its initial shape, attesting the good flexibility and redox stability of the Ce95Cu5 catalyst. Nevertheless, the defect band is slightly more intense after each cycle of reduction and oxidation (as shown in Fig. 8 F). This behavior indicates that exposure to increasing concentrations of CO is associated with the formation of more and more structural defects, especially of the Frenkel type (D1). This effect is

likely a consequence of the higher degree of stress which the structure undergoes upon increasing CO concentration, which generates new interstitial sites able to accommodate a displaced oxygen ion.

Finally, the evolution of the Raman spectrum during cooling in reducing atmosphere is displayed in Fig. 8 G. Despite the absence of gaseous O_2, the D3 band related to O_V nearly completely faded at RT. Since the complete refill of the vacancies has to be ruled out, a structural reorganization accounts for the disappearance of the D3 signal. This peculiar behavior supports the assignment of the D3 band to clusters of O_V. Indeed, when the catalyst is cooled below its light-off temperature, CO molecules are no longer able to remove oxygen from the surface; hence, the O_V clusters, which only form when the oxygen demand from the surface is high, are gradually refilled by bulk lattice oxygen. This phenomenon results in a more homogeneous dispersion of O_V, causing the disappearance of the D3 component linked to clusters. Moreover, this behavior evidences that lattice oxygen mobility in Ce95Cu5 is still high below 200 °C.

The latter outcome is confirmed by the Raman spectra collected at RT after the test, presented in Fig. 8 H. A remarkable growth of the whole defect band can be observed after the different reduction/oxidation cycles, pointing out the strong effect of CO oxidation on the oxide structure. An analogous behavior was also observed after CO oxidation in the presence of abundant gaseous O_2 [23]: therefore, the structural rearrangement is not simply related to the catalyst reduction, but rather to the involvement of lattice oxygen in CO oxidation, which occurs through a MvK mechanism in the presence of O_2. Interestingly, the defect band changes when the sample is exposed to air (Fig. 8 H), showing an increase of the D1 and D2 peaks. This means that oxygen can interact with the catalyst even at RT, refilling some of the numerous isolated O_V formed after cluster dispersion and generating new Frenkel defects (D1) and oxidized substitutional sites (D2). This behavior confirms the great lattice oxygen mobility and structural flexibility of Cu-doped ceria.

In the end, the combined spectroscopic approach employed here allowed to thoroughly investigate how copper addition affects the structural, chemical and catalytic properties of ceria. The beneficial effect of Cu-doping on ceria oxidizing activity stems from the synergistic cooperation of different sites, each one playing its own role during CO oxidation. In particular, four different copper species are present in the fresh Ce95Cu5 sample, as schematized in Fig. 9. Cu^+ ions at the catalyst surface (i), detected via XPS and in situ FTIR spectroscopy, promote CO adsorption and its following oxidation. A similar function can be also carried out by some very small clusters of metallic Cu at the catalyst surface (ii), detected via in situ FTIR, which are however oxidized to Cu^+ under reaction conditions at high temperature. Isolated Cu^{2+} monomers well-dispersed in the ceria matrix (iii), revealed via EPR, can foster oxygen transfer thanks to the coupling of the Cu^{2+}/Cu^+ and Ce^{4+}/Ce^{3+} redox cycles; the latter species may occupy the oxidized D2 sites observed in the Ce95Cu5 Raman spectrum. EPR also evidenced the presence of Cu^{2+} dimers (iv) in the bulk or sub-surface, which are able to strongly weaken the bonds of neighboring O^{2-} ions, improving the catalyst reducibility; in the proximity of such sites, O_V clusters may form in sufficiently reducing conditions, as revealed by the evolution of the D3 band during in situ Raman measurements. Additionally, lattice oxygen mobility is also affected by the presence of Frenkel pairs, as interstitial sites may provide a path for oxygen transfer.
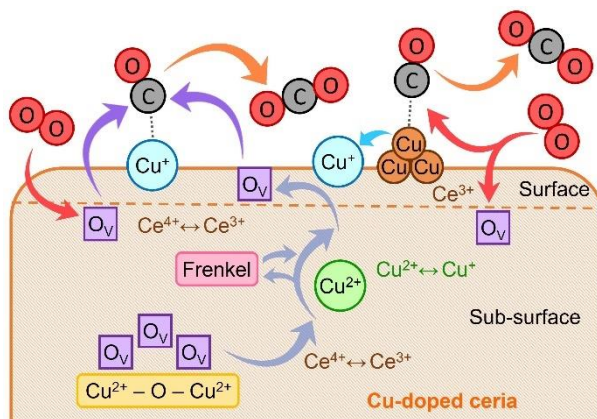
Fig. 9. Scheme describing different catalytic sites and mechanisms involved in CO oxidation over copper-doped ceria.

4. Conclusions

In the present work, a deep investigation of Cu-doped ceria was performed through complementary spectroscopic techniques (i.e. XPS, EPR, FTIR and Raman spectroscopy), in order to elucidate the remarkable catalytic activity of this mixed oxide towards CO oxidation. In fact, a 5 at.% copper doping leads to a 200 °C lower temperature required for CO oxidation with respect to pure ceria. The insertion of copper into ceria lattice results in the formation of various sites, which can synergistically cooperate during catalytic redox reactions. Surface copper is mainly in the Cu^+ form, although indications of the simultaneous presence of very small Cu^0 clusters were also obtained; both these species can effectively interact with gaseous reactants, e.g. promoting the adsorption of CO and the activation of molecular oxygen. At the same time, Cu species well-integrated in ceria bulk and sub-surface (such as the isolated Cu^{2+} monomers and dimers detected via EPR) improve the lattice oxygen mobility, making the structure so flexible that it can change even at RT. The enhanced mobility can be attributed to the coupling of the Cu^{2+}/Cu^+ and Ce^{4+}/Ce^{3+} redox cycles, the generation of oxygen vacancies or other defects, and the weakening of the Ce – O bonds upon Cu doping. All these effects allow to extend the quantity of catalyst able to actively take part in oxidation reactions, involving a sub-surface layer in the redox phenomena. Such a capability is responsible for the superior oxidizing activity of the mixed oxide and makes the catalyst particularly suitable for those applications in which gaseous O_2 may temporarily lack. All these outcomes also point out the need of systematic multi-technique investigations for the full understanding of complex catalytic systems.

Declaration of interest

The authors declare no competing interests.

Appendix A. Supplementary data

Supplementary material related to this article can be found, in the online version, at doi:

References

[1] T. Montini, M. Melchionna, M. Monai, P. Fornasiero, Fundamentals and Catalytic Applications of CeO_2-Based Materials, Chem. Rev. 116 (2016) 5987–6041. https://doi.org/10.1021/acs.chemrev.5b00603.

[2] T. Andana, K.G. Rappé, N.C. Nelson, F. Gao, Y. Wang, Selective catalytic reduction of NO_x with NH_3 over Ce-Mn oxide and Cu-SSZ-13 composite catalysts – Low temperature enhancement, Appl. Catal. B Environ. 316 (2022). https://doi.org/10.1016/j.apcatb.2022.121522.

[3] Q. Wang, K.L. Yeung, M.A. Bañares, Ceria and its related materials for VOC catalytic combustion: A review, Catal. Today. 356 (2020) 141–154. https://doi.org/10.1016/j.cattod.2019.05.016.

[4] S. Liu, X. Wu, D. Weng, R. Ran, Ceria-based catalysts for soot oxidation: A review, J. Rare Earths. 33 (2015) 567–590. https://doi.org/10.1016/S1002-0721(14)60457-9.

[5] Y. Sun, F. Polo-Garzon, Z. Bao, J. Moon, Z. Huang, H. Chen, Z. Chen, Z. Yang, M. Chi, Z. Wu, J. Liu, S. Dai, Manipulating Copper Dispersion on Ceria for Enhanced Catalysis: A Nanocrystal-Based Atom-Trapping Strategy, Adv. Sci. 9 (2022) 1–9. https://doi.org/10.1002/advs.202104749.

[6] J.D. Jiménez, L.E. Betancourt, M. Danielis, H. Zhang, F. Zhang, I. Orozco, W. Xu, J. Llorca, P. Liu, A. Trovarelli, J.A. Rodríguez, S. Colussi, S.D. Senanayake, Identification of Highly Selective Surface Pathways for Methane Dry Reforming Using Mechanochemical Synthesis of Pd-CeO_2, ACS Catal. 12 (2022) 12809–12822. https://doi.org/10.1021/acscatal.2c01120.

[7] J. Pan, S. Wang, A. Chen, Y. Chen, M. Wang, Y. Chen, Visible-light-active mesoporous ceria (CeO_2) nanospheres for improved photocatalytic performance, J. Alloys Compd. 898 (2022) 162895. https://doi.org/10.1016/J.JALLCOM.2021.162895.

[8] E.M. Sala, N. Mazzanti, M.B. Mogensen, C. Chatzichristodoulou, Current understanding of ceria surfaces for

CO₂ reduction in SOECs and future prospects – A review, Solid State Ionics. 375 (2022) 115833. https://doi.org/10.1016/j.ssi.2021.115833.

[9]   M. Giuliano, M.C. Valsania, P. Ticali, E. Sartoretti, S. Morandi, S. Bensaid, G. Ricchiardi, M. Sgroi, Characterization of the Evolution of Noble Metal Particles in a Commercial Three-Way Catalyst: Correlation between Real and Simulated Ageing, Catalysts. 11 (2021). https://doi.org/10.3390/catal11020247.

[10]   Y. Wang, Z. Chen, P. Han, Y. Du, Z. Gu, X. Xu, G. Zheng, Single-Atomic Cu with Multiple Oxygen Vacancies on Ceria for Electrocatalytic CO₂ Reduction to CH4, ACS Catal. 8 (2018) 7113–7119. https://doi.org/10.1021/acscatal.8b01014.

[11]   D. Mukherjee, B.G. Rao, B.M. Reddy, CO and soot oxidation activity of doped ceria: Influence of dopants, Appl. Catal. B Environ. 197 (2016) 105–115. https://doi.org/10.1016/j.apcatb.2016.03.042.

[12]   S.C. Rood, O. Pastor-Algaba, A. Tosca-Princep, B. Pinho, M. Isaacs, L. Torrente-Murciano, S. Eslava, Synergistic Effect of Simultaneous Doping of Ceria Nanorods with Cu and Cr on CO Oxidation and NO Reduction, Chem. – A Eur. J. 27 (2021) 2165–2174. https://doi.org/10.1002/CHEM.202004623.

[13]   M. Konsolakis, The role of Copper–Ceria interactions in catalysis science: Recent theoretical and experimental advances, Appl. Catal. B Environ. 198 (2016) 49–66. https://doi.org/10.1016/j.apcatb.2016.05.037.

[14]   E. Sartoretti, C. Novara, F. Giorgis, M. Piumetti, S. Bensaid, N. Russo, D. Fino, In situ Raman analyses of the soot oxidation reaction over nanostructured ceria-based catalysts, Sci. Rep. 9 (2019) 3875. https://doi.org/10.1038/s41598-019-39105-5.

[15]   M. Lykaki, E. Pachatouridou, S.A.C. Carabineiro, E. Iliopoulou, C. Andriopoulou, N. Kallithrakas-Kontos, S. Boghosian, M. Konsolakis, Ceria nanoparticles shape effects on the structural defects and surface chemistry: Implications in CO oxidation by Cu/CeO₂ catalysts, Appl. Catal. B Environ. 230 (2018) 18–28. https://doi.org/10.1016/j.apcatb.2018.02.035.

[16]   C. Papadopoulos, K. Kappis, J. Papavasiliou, J. Vakros, M. Kuśmierz, W. Gac, Y. Georgiou, Y. Deligiannakis, G. Avgouropoulos, Copper-promoted ceria catalysts for CO oxidation reaction, Catal. Today. 355 (2020) 1–7. https://doi.org/10.1016/j.cattod.2019.06.078.

[17]   M. Dosa, M.J. Marin-figueredo, E. Sartoretti, C. Novara, F. Giorgis, S. Bensaid, D. Fino, N. Russo, M. Piumetti, Cerium-Copper Oxides Synthesized in a Multi-Inlet Vortex Reactor as Effective Nanocatalysts for CO and Ethene Oxidation Reactions, Catalysts. 12 (2022). https://doi.org/10.3390/catal12040364.

[18]   F. Sapio, F. Millo, D. Fino, A. Monteverde, E. Sartoretti, A. Bianco, L. Postrioti, A. Tarabocchia, G. Buitoni, G. Brizi, Experimental and Numerical Analysis of Latest Generation Diesel Aftertreatment Systems, SAE Tech. Pap. Ser. 1 (2019). https://doi.org/10.4271/2019-24-0142.

[19]   J. Graciani, K. Mudiyanselage, F. Xu, A.E. Baber, J. Evans, S.D. Senanayake, D.J. Stacchiola, P. Liu, J. Hrbek, J. Fernández Sanz, J.A. Rodriguez, Highly active copper-ceria and copper-ceria-titania catalysts for methanol synthesis from CO₂, Science (80-.). 345 (2014) 546–550. https://doi.org/10.1126/SCIENCE.1253057/SUPPL_FILE/GRACIANI.SM.PDF.

[20]   A. Davó-Quiñonero, E. Bailón-García, S. López-Rodríguez, J. Juan-Juan, D. Lozano-Castelló, M. García-Melchor, F.C. Herrera, E. Pellegrin, C. Escudero, A. Bueno-López, Insights into the Oxygen Vacancy Filling Mechanism in CuO/CeO₂ Catalysts: A Key Step Toward High Selectivity in Preferential CO Oxidation, ACS Catal. 10 (2020) 6532–6545. https://doi.org/10.1021/acscatal.0c00648.

[21]   M. Konsolakis, M. Lykaki, Recent advances on the rational design of nonprecious metal oxide catalysts exemplified by CuOₓ/CeO₂ binary system: Implications of size, shape and electronic effects on intrinsic reactivity and metal-support interactions, Catalysts. 10 (2020). https://doi.org/10.3390/catal10020160.

[22]   J.S. Elias, K.A. Stoerzinger, W.T. Hong, M. Risch, L. Giordano, A.N. Mansour, Y. Shao-Horn, In situ spectroscopy and mechanistic insights into CO oxidation on transition-metal-substituted ceria nanoparticles, ACS Catal. 7 (2017) 6843–6857. https://doi.org/10.1021/acscatal.7b01600.

[23]   E. Sartoretti, C. Novara, M. Fontana, F. Giorgis, M. Piumetti, S. Bensaid, N. Russo, D. Fino, New insights on the defect sites evolution during CO oxidation over doped ceria nanocatalysts probed by in situ Raman spectroscopy, Appl. Catal. A Gen. 596 (2020) 117517. https://doi.org/10.1016/j.apcata.2020.117517.

[24]   J. Zhang, K. Wu, J. Xiong, Q. Ren, J. Zhong, H. Cai, H. Huang, P. Chen, J. Wu, L. Chen, M. Fu, D. Ye, Static and dynamic quantification tracking of asymmetric oxygen vacancies in copper-ceria catalysts with superior catalytic activity, Appl. Catal. B Environ. 316 (2022) 121620. https://doi.org/10.1016/j.apcatb.2022.121620.

[25]   H. Zhu, Y. Chen, Z. Wang, W. Liu, L. Wang, Catalytic oxidation of CO over mesoporous copper-doped ceria catalysts via a facile CTAB-assisted synthesis, RCS Adv. (2018) 14888–14897. https://doi.org/10.1039/c8ra02327a.

[26]   M. Dosa, M. Piumetti, S. Bensaid, N. Russo, D. Fino, Novel Mn–Cu-Containing CeO₂ Nanopolyhedra for the Oxidation of CO and Diesel Soot (Part II): Effect of Oxygen Concentration on the Catalytic Activity, Catal. Letters. 149 (2019) 107–118. https://doi.org/10.1007/s10562-018-2591-1.

[27]   K. Kappis, J. Papavasiliou, Influence of the Hydrothermal Parameters on the Physicochemical Characteristics of Cu−Ce Oxide Nanostructures, ChemCatChem. 11 (2019) 4765–4776. https://doi.org/10.1002/cctc.201901108.

[28]   W. Li, Y. Hu, H. Jiang, N. Jiang, W. Bi, C. Li, Litchi-peel-like hierarchical hollow copper-ceria microspheres: aerosol-assisted synthesis and high activity and stability for catalytic CO oxidation, Nanoscale. 10 (2018)

22775–22786. https://doi.org/10.1039/C8NR04642E.

[29]   M. Dosa, M. Piumetti, S. Bensaid, T. Andana, C. Novara, F. Giorgis, D. Fino, N. Russo, Novel Mn–Cu-Containing CeO_2 Nanopolyhedra for the Oxidation of CO and Diesel Soot: Effect of Dopants on the Nanostructure and Catalytic Activity, Catal. Letters. 148 (2018) 298–311. https://doi.org/10.1007/s10562-017-2226-y.

[30]   B. Wang, H. Zhang, W. Xu, X. Li, W. Wang, L. Zhang, Y. Li, Z. Peng, F. Yang, Z. Liu, Nature of Active Sites on Cu−CeO_2 Catalysts Activated by High- Temperature Thermal Aging, ACS Catal. 10 (2020) 12385–12392.

[31]   A. Trovarelli, J. Llorca, Ceria Catalysts at Nanoscale: How Do Crystal Shapes Shape Catalysis?, ACS Catal. 7 (2017) 4716–4735. https://doi.org/10.1021/acscatal.7b01246.

[32]   A. Pereira, M. Blouin, A. Pillonnet, D. Guay, Structure and valence properties of ceria films synthesized by laser ablation under reducing atmosphere, Mater. Res. Express. 1 (2014). https://doi.org/10.1088/2053-1591/1/1/015704.

[33]   E. Sartoretti, F. Martini, M. Piumetti, S. Bensaid, N. Russo, D. Fino, Nanostructured Equimolar Ceria-Praseodymia for Total Oxidations in Low-O_2 Conditions, Catalysts. 10 (2020) 1–16. https://doi.org/10.3390/catal10020165.

[34]   Z. Li, K. Werner, K. Qian, R. You, A. Płucienik, A. Jia, L. Wu, L. Zhang, H. Pan, H. Kuhlenbeck, S. Shaikhutdinov, W. Huang, H.J. Freund, Oxidation of Reduced Ceria by Incorporation of Hydrogen, Angew. Chemie - Int. Ed. 58 (2019) 14686–14693. https://doi.org/10.1002/anie.201907117.

[35]   S. Ballauri, E. Sartoretti, M. Hu, C. D'Agostino, Z. Ge, L. Wu, C. Novara, F. Giorgis, M. Piumetti, D. Fino, N. Russo, S. Bensaid, Praseodymium doping in ceria-supported palladium nanocatalysts as an effective strategy to minimize the inhibiting effects of water during methane oxidation, Appl. Catal. B Environ. 320 (2023) 121898. https://doi.org/10.1016/j.apcatb.2022.121898.

[36]   L. Chen, Y. Tang, L. Cui, C. Ouyang, S. Shi, Charge transfer and formation of Ce^{3+} upon adsorption of metal atom M (M = Cu, Ag Au) on CeO_2 (100) surface, 234 (2013). https://doi.org/10.1016/j.jpowsour.2013.01.121.

[37]   F. Salomone, G. Bonura, F. Frusteri, M. Castellino, M. Fontana, A.M. Chiodoni, N. Russo, R. Pirone, S. Bensaid, Physico-Chemical Modifications Affecting the Activity and Stability of Cu-Based Hybrid Catalysts during the Direct Hydrogenation of Carbon Dioxide into Dimethyl-Ether, Materials (Basel). 15 (2022) 7774. https://doi.org/10.3390/ma15217774.

[38]   M.C. Biesinger, Advanced analysis of copper X-ray photoelectron spectra, Surf. Interface Anal. (2017) 1325–1334. https://doi.org/10.1002/sia.6239.

[39]   C. Meng, T. Chen, C. Fang, Y. Huang, P. Hu, Y. Tong, T. Bian, J. Zhang, Z. Wang, A. Yuan, Multiple Active Sites: Lithium Storage Mechanism of Cu-TCNQ as an Anode Material for Lithium-Ion Batteries, Chem. - An Asian J. 14 (2019) 4289–4295. https://doi.org/10.1002/ASIA.201901190.

[40]   W.W. Wang, W.Z. Yu, P.P. Du, H. Xu, Z. Jin, R. Si, C. Ma, S. Shi, C.J. Jia, C.H. Yan, Crystal Plane Effect of Ceria on Supported Copper Oxide Cluster Catalyst for CO Oxidation: Importance of Metal-Support Interaction, ACS Catal. 7 (2017) 1313–1329. https://doi.org/10.1021/acscatal.6b03234.

[41]   S. Dey, G. Chandra Dhal, Controlling carbon monoxide emissions from automobile vehicle exhaust using copper oxide catalysts in a catalytic converter, Mater. Today Chem. 17 (2020) 100282. https://doi.org/10.1016/j.mtchem.2020.100282.

[42]   R.M. Rakhmatullin, V. V. Semashko, S.L. Korableva, A.G. Kiiamov, A.A. Rodionov, R. Tschaggelar, J.A. van Bokhoven, C. Paun, EPR study of ceria nanoparticles containing different concentration of Ce^{3+} ions, Mater. Chem. Phys. 219 (2018) 251–257. https://doi.org/10.1016/j.matchemphys.2018.08.028.

[43]   J. Chen, Y. Zhan, J. Zhu, C. Chen, X. Lin, Q. Zheng, The synergetic mechanism between copper species and ceria in NO abatement over Cu/CeO_2 catalysts, Appl. Catal. A Gen. 377 (2010) 121–127. https://doi.org/10.1016/j.apcata.2010.01.027.

[44]   R. Kydd, W.Y. Teoh, K. Wong, Y. Wang, J. Scott, Q.H. Zeng, A.B. Yu, J. Zou, R. Amal, Flame-synthesized ceria-supported copper dimers for preferential oxidation of CO, Adv. Funct. Mater. 19 (2009) 369–377. https://doi.org/10.1002/adfm.200801211.

[45]   K. Wong, Q. Zeng, A. Yu, Interfacial synergistic effect of the Cu monomer or CuO dimer modified CeO_2(111) catalyst for CO oxidation, Chem. Eng. J. 174 (2011) 408–412. https://doi.org/10.1016/j.cej.2011.09.020.

[46]   A. Aboukaïs, A. Bennani, C.F. Aïssi, G. Wrobel, M. Guelton, J.C. Vedrine, Highly resolved electron paramagnetic resonance spectrum of copper(II) ion pairs in CuCe oxide, J. Chem. Soc. Faraday Trans. 88 (1992) 615–620. https://doi.org/10.1039/FT9928800615.

[47]   F. Wang, R. Büchel, A. Savitsky, M. Zalibera, D. Widmann, S.E. Pratsinis, W. Lubitz, F. Schüth, In Situ EPR Study of the Redox Properties of CuO-CeO_2 Catalysts for Preferential CO Oxidation (PROX), ACS Catal. 6 (2016) 3520–3530. https://doi.org/10.1021/acscatal.6b00589.

[48]   S. Bensaid, N. Russo, Low temperature DPF regeneration by delafossite catalysts, Catal. Today. 176 (2011) 417–423. https://doi.org/10.1016/j.cattod.2010.11.020.

[49]   S. Ballauri, E. Sartoretti, C. Novara, F. Giorgis, M. Piumetti, D. Fino, N. Russo, S. Bensaid, Wide range temperature stability of palladium on ceria-praseodymia catalysts for complete methane oxidation, Catal. Today. 390–391 (2022) 185–197. https://doi.org/10.1016/j.cattod.2021.11.035.

[50] S. Loridant, Raman spectroscopy as a powerful tool to characterize ceria-based catalysts, Catal. Today. (2020) 1–14. https://doi.org/10.1016/j.cattod.2020.03.044.

[51] S. Agarwal, X. Zhu, E.J.M. Hensen, L. Lefferts, B.L. Mojet, Defect chemistry of ceria nanorods, J. Phys. Chem. C. 118 (2014) 4131–4142. https://doi.org/10.1021/jp409989y.

[52] M. Verma, V. Kumar, A. Katoch, Sputtering based synthesis of CuO nanoparticles and their structural, thermal and optical studies, Mater. Sci. Semicond. Process. 76 (2018) 55–60. https://doi.org/10.1016/j.mssp.2017.12.018.

[53] C. Andriopoulou, A. Trimpalis, K.C. Petallidou, A. Sgoura, A.M. Efstathiou, S. Boghosian, Structural and Redox Properties of $Ce_{1-x}Zr_xO_{2-\delta}$ and $Ce_{0.8}Zr_{0.15}RE_{0.05}O_{2-\delta}$ (RE: La, Nd, Pr, Y) Solids Studied by High Temperature in Situ Raman Spectroscopy, J. Phys. Chem. C. 121 (2017) 7931–7943. https://doi.org/10.1021/acs.jpcc.7b00515.

[54] T. Vinodkumar, B.G. Rao, B.M. Reddy, Influence of isovalent and aliovalent dopants on the reactivity of cerium oxide for catalytic applications, Catal. Today. 253 (2015) 57–64. https://doi.org/10.1016/j.cattod.2015.01.044.

[55] E. Sartoretti, C. Novara, A. Chiodoni, F. Giorgis, M. Piumetti, S. Bensaid, N. Russo, D. Fino, Nanostructured ceria-based catalysts doped with La and Nd: How acid-base sites and redox properties determine the oxidation mechanisms, Catal. Today. 390–391 (2021) 117–134. https://doi.org/10.1016/j.cattod.2021.11.040.

[56] K. Kappis, C. Papadopoulos, J. Papavasiliou, J. Vakros, Y. Georgiou, Y. Deligiannakis, G. Avgouropoulos, Tuning the catalytic properties of copper-promoted nanoceria via a hydrothermal method, Catalysts. 9 (2019). https://doi.org/10.3390/catal9020138.

[57] C. Binet, M. Daturi, Methanol as an IR probe to study the reduction process in ceria-zirconia mixed compounds, Catal. Today. 70 (2001) 155–167. https://doi.org/10.1016/S0920-5861(01)00415-1.

[58] P.K. Huttunen, D. Labadini, S.S. Hafiz, S. Gokalp, E.P. Wolff, S.M. Martell, M. Foster, DRIFTS investigation of methanol oxidation on CeO_2 nanoparticles, Appl. Surf. Sci. 554 (2021) 149518. https://doi.org/10.1016/j.apsusc.2021.149518.

[59] Z. Zhang, Y. Wang, J. Lu, J. Zhang, M. Li, X. Liu, F. Wang, Pr-Doped CeO_2 Catalyst in the Prins Condensation-Hydrolysis Reaction: Are All of the Defect Sites Catalytically Active?, ACS Catal. 8 (2018) 2635–2644. https://doi.org/10.1021/acscatal.7b04500.

[60] Z. Wu, M. Li, D.R. Mullins, S.H. Overbury, Probing the surface sites of CeO_2 nanocrystals with well-defined surface planes via methanol adsorption and desorption, ACS Catal. 2 (2012) 2224–2234. https://doi.org/10.1021/cs300467p.

[61] B. Liu, C. Li, G. Zhang, X. Yao, S.S.C. Chuang, Z. Li, Oxygen Vacancy Promoting Dimethyl Carbonate Synthesis from CO_2 and Methanol over Zr-Doped CeO_2 Nanorods, ACS Catal. 8 (2018) 10446–10456. https://doi.org/10.1021/acscatal.8b00415.

[62] A. Chen, X. Yu, Y. Zhou, S. Miao, Y. Li, S. Kuld, J. Sehested, J. Liu, T. Aoki, S. Hong, M.F. Camellone, S. Fabris, J. Ning, C. Jin, C. Yang, A. Nefedov, C. Wöll, Y. Wang, W. Shen, Structure of the catalytically active copper–ceria interfacial perimeter, Nat. Catal. 2 (2019) 334–341. https://doi.org/10.1038/s41929-019-0226-6.

[63] L. Kang, B. Wang, Q. Bing, M. Zalibera, R. Büchel, R. Xu, Q. Wang, Y. Liu, D. Gianolio, C.C. Tang, E.K. Gibson, M. Danaie, C. Allen, K. Wu, S. Marlow, L. Sun, Q. He, S. Guan, A. Savitsky, J.J. Velasco-vélez, J. Callison, C.W.M. Kay, Adsorption and activation of molecular oxygen over atomic copper(I/II) site on ceria, (2020) 17–19. https://doi.org/10.1038/s41467-020-17852-8.

[64] Y. Tang, L. Dong, C. Deng, M. Huang, B. Li, H. Zhang, In situ FT-IR investigation of CO oxidation on CuO/TiO_2 catalysts, Catal. Commun. 78 (2016) 33–36. https://doi.org/10.1016/j.catcom.2016.02.001.

[65] K. Mudiyanselage, H.Y. Kim, S.D. Senanayake, A.E. Baber, P. Liu, D. Stacchiola, Probing adsorption sites for CO on ceria, Phys. Chem. Chem. Phys. 15 (2013) 15856–15862. https://doi.org/10.1039/c3cp52295d.

[66] M. Manzoli, R. Di Monte, F. Boccuzzi, S. Coluccia, J. Kašpar, CO oxidation over CuO_x-CeO_2-ZrO_2 catalysts: Transient behaviour and role of copper clusters in contact with ceria, Appl. Catal. B Environ. 61 (2005) 192–205. https://doi.org/10.1016/j.apcatb.2005.05.005.

[67] K. Mudiyanselage, W. An, F. Yang, P. Liu, D.J. Stacchiola, Selective molecular adsorption in sub-nanometer cages of a Cu_2O surface oxide, Phys. Chem. Chem. Phys. 15 (2013) 10726–10731. https://doi.org/10.1039/c3cp50522g.